



ORIGINAL ARTICLE

Synthesis of eco-friendly porous g-C₃N₄/SiO₂/SnO₂ composite with excellent visible-light responsive photocatalysis



Li Peng^a, Ren-rong Zheng^a, Da-wei Feng^{b,*}, Hui Yu^{a,*}, Xiang-ting Dong^a

^a School of Chemistry & Environmental Engineering, Changchun University of Science and Technology, Changchun 130022, PR China

^b Changchun University of Science and Technology Science Park, Changchun 130022, PR China

Received 28 April 2019; accepted 26 July 2019

Available online 6 August 2019

KEYWORDS

Disorder mesoporous SnO₂ aerogel;
G-C₃N₄;
Hard template method;
Photocatalytic;
Visible-light

Abstract Forming eco-friendly heterojunction photocatalysts is excellent method to accelerate the separation rate of photogenerated charge carriers, which is attracting more and more attention. In this study, a novel and stable disordered porous g-C₃N₄/SiO₂/SnO₂ (DOP-CSiSn) heterojunction composites was fabricated by a sol-gel hard template method, and the optimal g-C₃N₄ doped ratio was adjusted in DOP-CSiSn. The DOP-CSiSn photocatalyst had the much larger specific surface area and disordered porous structure, which exhibited strong photocatalytic effect to degrade Rhodamine B (RhB), Methylene blue (MB) and Methyl orange (MO) under visible light. When the g-C₃N₄ doping content was 30 wt%, the highest photocatalytic activities were obtained, and the degradation rate of MB and MO were 99.73% and 95.58% after 50 min, respectively. Degradation rate of RhB was 95.10% after 90 min. Photocatalytic degradation rate of organic pollutants were still more than 90% after six time consecutive cycles, the composite had wonderful stability and potential value in environmental purification.

© 2019 Production and hosting by Elsevier B.V. on behalf of King Saud University. This is an open access article under the CC BY-NC-ND license (<http://creativecommons.org/licenses/by-nc-nd/4.0/>).

1. Introduction

The global population growth led to sustained growth in energy demand, which induced a series of environmental issues. The environmental problems solving needs to be started from advanced technologies of green fuel production and effective elimination of harmful pesticides and organic pollutants (Wang and Wu, 2013). Since Fujishima and Honda reported that TiO₂ electrode could produce H₂ and O₂ in 1972, the semiconductor-based photocatalysis seemed to be a

* Corresponding authors.

E-mail addresses: custkij@163.com (D.-w. Feng), yh2001101@163.com (H. Yu).

Peer review under responsibility of King Saud University.



versatile concept of green technology because of their capacities for water decontamination and water splitting (Zheng and Yang, 2018; Yan et al., 2018). The wolframite and titanate heterostructure materials have been used to degrade organic pollutants (Zhao et al., 2018; Mohnamed et al., 2012; Kumar et al., 2014). The most of oxide semiconductors have been used as photocatalysis, such as TiO_2 (Jallouli et al., 2019; Nadarajan et al., 2018; Zheng et al., 2017; Wu et al., 2017; Hao et al., 2017), ZnO (Liu et al., 2017; Rashid et al., 2014), SnO_2 (You et al., 2013; Wu et al., 2011), Fe_2O_3 (Tian et al., 2014; Xu et al., 2018), CdSe (Shi et al., 2017) etc.

Due to widespread use, the tin oxide (SnO_2) has aroused people's attention. SnO_2 is a wide band gap (3.6 eV) n-type semiconductor (Rakibuddin et al., 2017; Zhang et al., 2013), which has been widely used in photo-catalytic degradation of organic dyes (Li et al., 2013), rechargeable lithium ion batteries (Reddy et al., 2016; Chen et al., 2017), gas sensors (Lin et al., 2015; Du et al., 2015; Qi et al., 2014; Liu et al., 2010), fuel sensitized solar cells (Son et al., 2015) and supercapacitor (Liu et al., 2014). Davis et al. (Davis et al., 2012) successfully prepared ZnO-SnO_2 nanocomposites photocatalysts. Huang et al. (2013) prepared ZnO nanorod- SnO_2 nanoparticle (ZnO NR- SnO_2 NPs) heterostructures through a simple way, the RhB degradation efficiency was 78% after 60 min. Kar et al. (2012) prepared SnO_2/CdS composite, and reported its photocatalytic properties, the photocatalytic degradation rate of Congo red dye was found to be 97% under UV light irradiation. Park et al. (2014) synthesized hierarchical mesoporous SnO_2 spheres which showed high photocatalytic properties under UV light. Due to the broad energy bandgap, SnO_2 can only be used as a active photocatalyst under ultraviolet light irradiation. It is all known that the UV region occupies only about 4% of all solar spectrum, while the visible light accounts for 45% of all solar spectrum. In order to broaden the applications of SnO_2 photocatalyst, visible light response must be achieved. Therefore, the energy band of SnO_2 needs to be modified. In order to reduce the band gap, there are three conventional strategies, which includes modifying of valence band, adjusting of conduction band and continuous modulation of valence and conduction bands. Many attempts have been made to improve visible-light photocatalysis of SnO_2 by doping with metal and non-metal. The purpose of these methods are achieve efficient separation of electron-holes by designing to construct a heterostructure and change the direction of electron transfer.

The non-metal doping has achieved remarkable results in recent years. For example, graphene and other carbon materials were used as absorbing material, electrochemical, which were also used to enhance the conductivity of semiconductor to evolve its response. But graphene requires complex processing procedures (Yang et al., 2018; Xia et al., 2018). The graphitic carbon nitride ($\text{g-C}_3\text{N}_4$) is an ideal non-metal. The $\text{g-C}_3\text{N}_4$ can be applied to SnO_2 band modification. As a perfect polymer n-type semiconductor, $\text{g-C}_3\text{N}_4$ attracted a lot of attention in degradation of organic pollutants (Jiang et al., 2015). The band gap of $\text{g-C}_3\text{N}_4$ is 2.73 eV (Thomas et al., 2008; Naseri et al., 2017), which indicates that the response wavelength of $\text{g-C}_3\text{N}_4$ is up to 450 nm. $\text{g-C}_3\text{N}_4$ has appropriate band gap to absorb the visible-light (He et al., 2017; Wen et al., 2017; Wei et al., 2017; Wang et al., 2017; Yu et al., 2017;

Zhao et al., 2017; Zhou et al., 2018), it can be easily prepared by calcining of melamine, urea and cyanamide (Wang et al., 2014; Kuang et al., 2015) which has been used in the field of photocatalysts. Kong et al. (2016) prepared low cost $\text{Ni/g-C}_3\text{N}_4$ photocatalyst, and 4318 $\mu\text{molg}^{-1} \text{h}^{-1}$ H_2 production rate was obtained when Ni was loaded to 7.40 wt%. However, the photocatalytic efficiency of $\text{g-C}_3\text{N}_4$ is still limited because of relatively fast recombination rate of photogenerated electron-hole pairs. In addition, the less surface area reduces absorption efficiency of $\text{g-C}_3\text{N}_4$ to visible-light. Therefore, $\text{g-C}_3\text{N}_4$ can be doped in porous SnO_2 matrix as visible light driven photocatalysts. On the other hand, the more active sites are provided by porous SnO_2 .

In the current work, we successfully prepared porous $\text{g-C}_3\text{N}_4/\text{SiO}_2/\text{SnO}_2$ composites by sol-gel method. The prepared $\text{g-C}_3\text{N}_4/\text{SiO}_2/\text{SnO}_2$ was characterized through powder X-ray diffraction (XRD), scanning electron microscopy (SEM), transmission electron microscope (TEM), ultraviolet-visible spectrum (UV-vis) and N_2 adsorption-desorption measurements. The prepared disordered porous $\text{g-C}_3\text{N}_4/\text{SiO}_2/\text{SnO}_2$ composite material had the higher photocatalytic activities to the decomposition of RhB, MB and MO under visible light (>420 nm) irradiation, which had potential applications in the decomposition of the organic pollutants.

2. Experimental

2.1. Materials

Tin (II) chloride dihydrate ($\text{SnCl}_2 \cdot 2\text{H}_2\text{O}$, A.R.) was produced by Xilong Chemical Research Institute in China. Tetraethyl silicate (TEOS, A.R.) was produced by Beijing Chemical Works Research Institute in China, melamine ($\text{C}_3\text{H}_6\text{N}_6$, A.R.) was produced by Tianjin Guangfu Fine Chemical Research Institute. Isopropyl alcohol ($\text{C}_3\text{H}_8\text{O}$, A.R.) and p-Benzoquinone ($\text{C}_6\text{H}_4\text{O}_2$, A.R.) were produced by Tianjin Fuyu Fine Chemical Co., Lt. Sodium oxalate ($\text{Na}_2\text{C}_2\text{O}_4$, A.R.) was produced by East China Reagent Factory. All reactants were analytical grade, and used without further purification. Deionized water and absolute alcohol were used throughout dissolution and filtration process.

2.2. Preparation of porous $\text{g-C}_3\text{N}_4/\text{SiO}_2/\text{SnO}_2$ composites

$\text{g-C}_3\text{N}_4$ was prepared according to the literature reported procedure (Sun et al., 2014). The detailed preparation process as follow: melamine was calcined at 550 °C with 10 °C·min⁻¹ heat rate for 2 h.

The $\text{g-C}_3\text{N}_4/\text{SiO}_2/\text{SnO}_2$ composite was synthesized by a sol-gel method. The detailed preparation process as follow: 11.283 g of $\text{SnCl}_2 \cdot 2\text{H}_2\text{O}$ was dissolved in 6.2 mL ethyl alcohol with stirring for 30 min, 3.8 mL of distilled water and different qualities $\text{g-C}_3\text{N}_4$ were added into the above solution with continue stirring for 2 h, and 4 mL of TEOS was added into the solution to form the gel. The gel was aged in room temperature for 24 h. The aged gel was soaked in deionized water to continue age at 70 °C for 2–4 d. The solvent of the gel was replaced by n-hexane solution at 50 °C for 2 d. The gel was dried, and calcined at 550 °C for 4 h with 1

°C·min⁻¹ heat rate. S₀, S₁, S₂, S₃ and S₄ were used for signing samples whose g-C₃N₄ doped quantity were 0 wt%, 10 wt%, 20 wt%, 30 wt% and 40 wt%, respectively.

2.3. Photodegradation character measurement

Under visible light, photocatalytic activities of the prepared g-C₃N₄/SiO₂/SnO₂ composites were evaluated through the photodegradation efficiency to organic dye solution (including RhB, MB and MO) at room temperature. 5 mg prepared composite was soaked in 95 mL deionized water, and 5 mL organic dye solution (0.0100 g/L) was added into the above solution. The mixture was continuously stirred for 1 h to ensure adsorption-desorption equilibrium of organic dye on the sample surfaces in the dark. Then, the mixture was radiated under a 500 W xenon lamp with continuously stirring. Current was set to 12.5 A, and light intensity was 150 Mw/cm². Every 10 min, 4 mL suspension liquid was taken out, and centrifuged to remove the particles of catalyst. The concentration of organic dye solution was determined by the maximum absorbance at fixed wavelength. Photocatalytic activities of the g-C₃N₄/SiO₂/SnO₂ was compared with SiO₂/SnO₂ and mechanical mixture (SiO₂/SnO₂ and g-C₃N₄) under the same experimental conditions.

2.4. Characterization

The morphologies of the samples were obtained by a scanning electron microscopy (SEM, JEOL JSM-5600L). Elemental composition of the g-C₃N₄/SiO₂/SnO₂ was obtained from energy dispersive x-ray spectroscopy (EDS) which was assembled on the SEM instrument. The microstructures were characterized using transmission electron microscope (TEM, JEOL 2010 TEM instrument). The X-ray diffraction (XRD) patterns of the prepared composites were recorded by a Siemens D5005 diffractometer using Cu-K α radiation ($\lambda = 1.5418 \text{ \AA}$ and operating at 30 kV and 20 mA). The ultraviolet-visible spectrum of sample was determined by an UV-1240 ultraviolet-visible spectrophotometer. Bet surface area (BET) and pores parameters were identified by physical adsorption of nitrogen on a Micromeritics ASAP2010M volumetric adsorption analyzer. Sample was degassed in vacuum at 573 K for 3 h before measurement. The pore size was computed using the BJH method.

3. Results and discussion

3.1. Structure characterization of porous g-C₃N₄/SiO₂/SnO₂ composites

The crystal phases of S₃ sample was confirmed by X-ray diffraction (XRD) analysis (Fig. 1). In the XRD pattern, the peaks at $2\theta = 26.6^\circ, 33.9^\circ, 37.9^\circ, 51.7^\circ, 57.8^\circ, 64.7^\circ, 78.7^\circ$ and 84.2° could be assigned to (1 1 0), (1 0 1), (2 0 0), (2 1 1), (0 0 2), (1 1 2), (3 2 1) and (4 1 0) planes of tetragonal rutile phase SnO₂ (JCPDS: 41-1445), respectively. The peaks at $2\theta = 26.6^\circ$ could also be assigned to (0 0 2) planes of g-C₃N₄ (JCPDS: 87-1526). There was no characteristic diffraction peak of SiO₂ in S₃ sample, it could be attributed to automatic

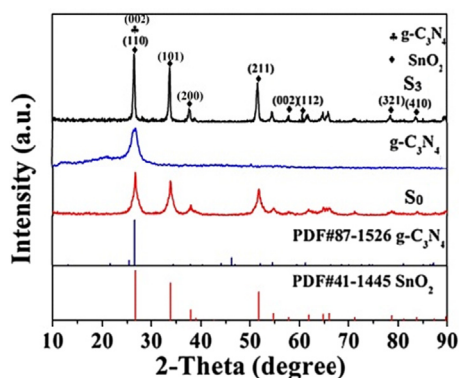


Fig. 1 XRD patterns of S₃, SnO₂ and g-C₃N₄ samples.

remediation of instrument because quartz sample trough was used in XRD measurement process. From Fig. 1, the g-C₃N₄ content has been assembled into the tetragonal rutile phase SnO₂ matrix.

Morphologies of the S₃ sample were characterized using SEM and TEM. From SEM image (Fig. 2a), the S₃ sample showed gel blocky structure with slice layer which was assembled with gel particles. Fig. 2b and Fig. 2c showed the TEM image and HRTEM image of S₃ sample, respectively. It could be clearly seen that surfaces of the gel particles were distributed with disordered loosened pores. The 0.336 nm and 0.347 nm interplanar crystal spacing could be corresponded to the (0 0 2) plane of g-C₃N₄ and (1 1 0) plane of SnO₂, which was consistent with the results of the XRD test. Elementary composition of S₃ sample was detected using EDS which was showed in Fig. 2d. Sn, O, C, N and Si elementary signals peaks were clearly seen in the EDS spectrum of S₃ sample which revealed the presence of Sn, O, C, N and Si in the prepared materials.

Fig. 3(a–e) showed SEM images of S₀, S₁, S₂, S₃ and S₄ composites, respectively. With the increase of content of g-C₃N₄, the particles in gel bulk structure became smaller. When the doped amount of g-C₃N₄ was 40 wt%, the morphology of the composite material changed significantly, and the gel bulk structure became an aggregate granular structure. It was attributed to which the superfluous g-C₃N₄ lead to gel bulk broke, and g-C₃N₄ reunite.

The nitrogen adsorption-desorption isotherms of S₃ sample was displayed in Fig. 4. It showed typical IV type isotherms with H1 hysteresis loop, which was the character of porous materials with cylindrical pores. From pore size distribution curves (Fig. 4 illustration), pore size distribution of S₃ sample was much narrow, which indicated that the prepared material had much homogeneous pores. Specific surface area of the S₃ sample was obtained using the BET method which was about 99.716 m²/g. Pore diameter was calculated by the BJH method which was about 3.56 nm.

3.2. Photocatalytic experiment

Photocatalytic activities of the prepared materials were evaluated through decomposition of MO, MB and RhB. Fig. 5(a–c) showed the degradation rates of S₀, S₁, S₂, S₃ and S₄ catalysts

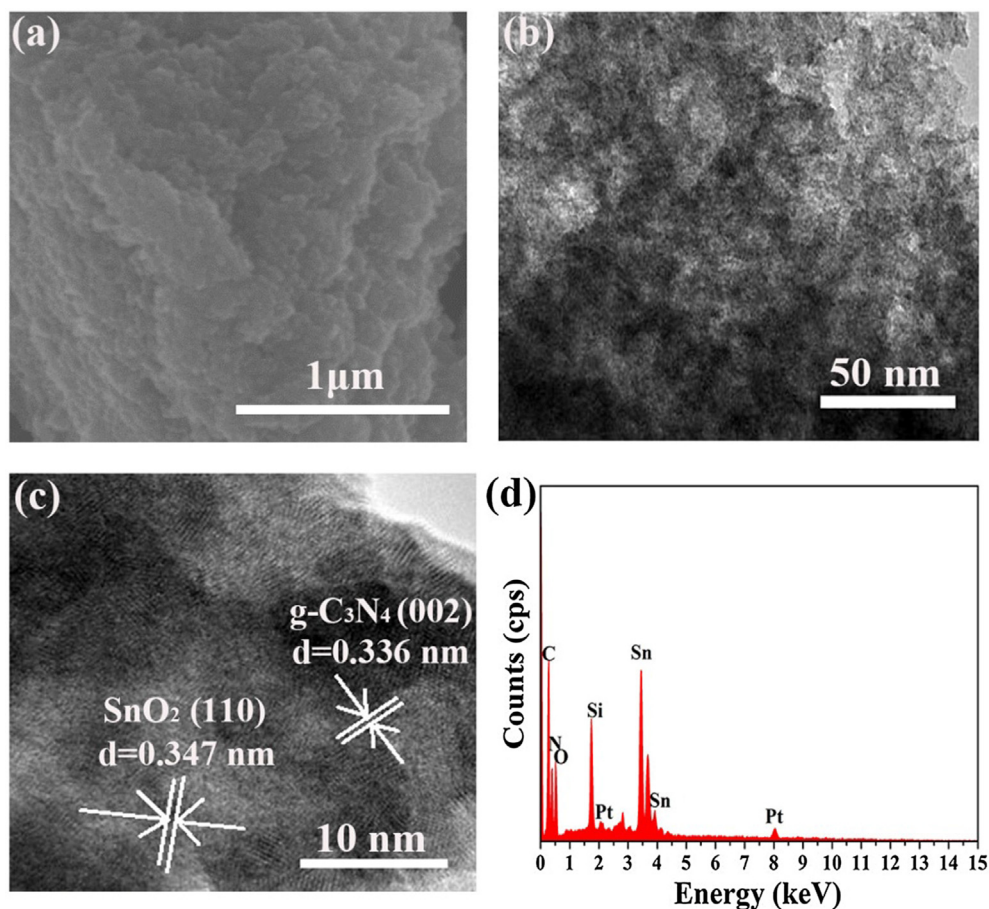


Fig. 2 (a) SEM image, (b) TEM image, (c) HRTEM image and (d) EDS spectrum of the prepared S_3 sample.

to MO, MB and RhB. For MO, the degradation rates of the five samples were 16.31%, 94.48%, 95.24%, 95.58% and 92.09% under visible light irradiation for 50 min, respectively. For MB, the degradation rates were 21.53%, 97.60%, 97.78%, 99.73% and 98.79% under visible light irradiation for 50 min, respectively. For RhB, the degradation rates respectively were 7.22%, 52.63%, 64.19%, 77.79% and 55.73% under visible light irradiation for 50 min, respectively. The prepared sample had the much better degradation effect to all three organic pollutants, and the degradation effects to MB and MO were much better than RhB. It could be seen that the S_3 sample had the best catalytic degradation effect to MB. From Fig. 5, the degradation rates of three organic pollutants increased with the increase of the $g\text{-C}_3\text{N}_4$ content, it reached the biggest when the $g\text{-C}_3\text{N}_4$ content was 30%, and it reduced when the $g\text{-C}_3\text{N}_4$ content was 40%. SnO_2 is a wide band gap (3.6 eV) n-type semiconductor which shows the photocatalytic activity under the UV-light, the band gap of $g\text{-C}_3\text{N}_4$ is 2.73 eV which has appropriate band gap to absorb the visible-light, however, the photocatalytic efficiency of $g\text{-C}_3\text{N}_4$ is limited because of relatively fast recombination rate of photogenerated electron-hole pairs. In $g\text{-C}_3\text{N}_4/\text{SiO}_2/\text{SnO}_2$ composite, the $g\text{-C}_3\text{N}_4$ can enhance the absorption capacity of visible light, and the porous SnO_2 matrix can weaken the recombination rate of photogenerated electron-hole and the agglomeration of $g\text{-C}_3\text{N}_4$,

their interaction improves the photocatalytic performance. Such, when $g\text{-C}_3\text{N}_4$ doped amount was increased, the absorption capacity of visible light was enhanced, and photocatalytic activities was enhanced. But, the agglomeration was happened (as Fig. 3-e) when the $g\text{-C}_3\text{N}_4$ doped amount was higher than 30%, it lead to the photocatalytic activities of the materials reduce.

From Fig. 6(a-c), S represented a mechanical mixture of $g\text{-C}_3\text{N}_4$ and $\text{SiO}_2/\text{SnO}_2$ matrix according to proportion of S_3 , which was tested under the same experimental conditions. Photocatalytic performance of the $g\text{-C}_3\text{N}_4/\text{SiO}_2/\text{SnO}_2$ samples were observably higher than that of $\text{SiO}_2/\text{SnO}_2$ and S samples. The degradation rates of S, S_0 , S_1 , S_2 , S_3 and S_4 samples to RhB were 76.19%, 21.65%, 86.20%, 90.93%, 95.10% and 77.23% under visible light irradiation after 90 min. With increasing of $g\text{-C}_3\text{N}_4$ doped amount, the photocatalytic activity was increased firstly, and then weakened. Photocatalytic activity reached the biggest when $g\text{-C}_3\text{N}_4$ doped amount was 30 wt%. When the doped amount of $g\text{-C}_3\text{N}_4$ was increased from 0 to 30 wt%, $g\text{-C}_3\text{N}_4$ was well dispersed in the matrix, which increased the contact area of $g\text{-C}_3\text{N}_4$ with the matrix, and also increased the reactive site, thereby improved photocatalytic performance of composite material. When $g\text{-C}_3\text{N}_4$ doped amount was exorbitant, dispersibility of $g\text{-C}_3\text{N}_4$ was decreased, and an aggregation would be occurred. It increased

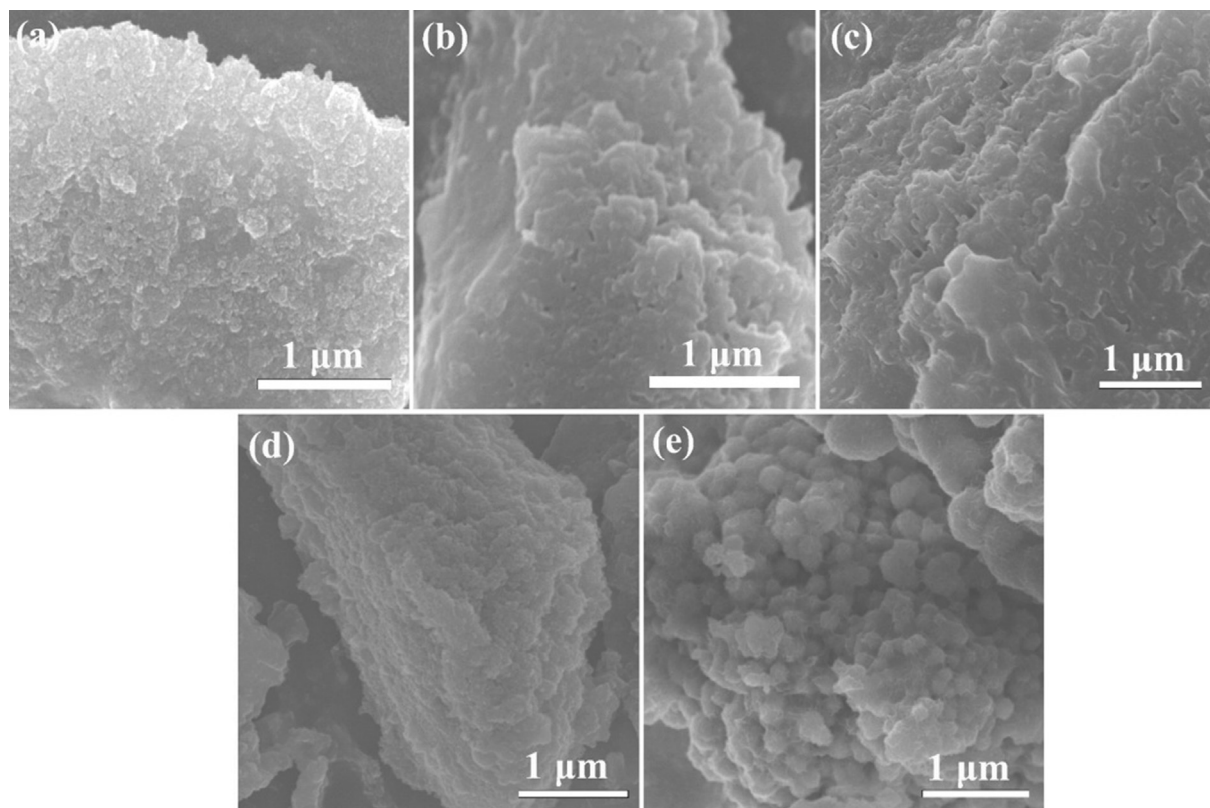


Fig. 3 SEM images of (a) S₀, (b) S₁, (c) S₂, (d) S₃ and (e) S₄ samples.

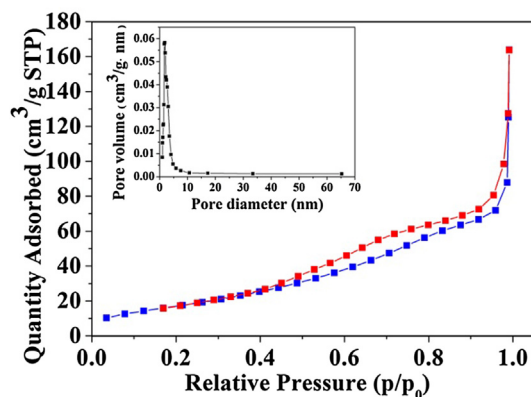


Fig. 4 Nitrogen adsorption-desorption isotherms and pore size distribution curves (inset) of the S₃ sample.

recombination probability of electron-hole, and photocatalytic effect was weakened. The characteristic absorption of MO, MB and RhB at $\lambda = 460$ nm, $\lambda = 660$ nm and $\lambda = 554$ nm were respectively monitored during photocatalytic degradation process. Fig. 6(d-f) were UV-visible absorption spectrum of MO, MB and RhB by catalysis of S₃ under the different visible light radiation time. MO and MB were almost completely degraded after 50 min, and RhB was completely degraded after

90 min. The photocatalytic activities of the prepared materials to RhB in 50 min was shown in supporting information Fig. S1.

The pseudo-first-order kinetic model (Formula (1)) was used to study the photocatalytic activity.

$$-\ln(C/C_0) = kt \quad (1)$$

where C_0 represents the initial concentration of pollutant before illumination, and C is the actual concentration at time t . When degrading MO as shown Fig. 7(a), the rate constants k of S₀, S₁, S₂, S₃ and S₄ for MO are 0.003 min⁻¹, 0.057 min⁻¹, 0.064 min⁻¹, 0.065 min⁻¹ and 0.050 min⁻¹, respectively. But the rate constants k of all samples for MB are 0.005 min⁻¹, 0.090 min⁻¹, 0.130 min⁻¹, 0.131 min⁻¹ and 0.0757 min⁻¹, respectively, as shown in Fig. 7 (b). When degrading RhB, the rate constants of catalysts are 0.003 min⁻¹, 0.025 min⁻¹, 0.029 min⁻¹, 0.036 min⁻¹ and 0.019 min⁻¹ for S₀, S₁, S₂, S₃ and S₄, which are consistent with the conclusion of Fig. 7(c).

Under visible light, MO, MB and RhB degradation cycling stability tests of the S₃ sample were researched, and the results were presented in Fig. 8. During the recycling experiment, the catalyst was collected by centrifugation, washed with deionized water, dried at 60 °C, and reused in the next cycles. For MO and MB degradation, the photocatalytic degradation rates of the S₃ sample were respectively maintained up 88.91% and 92.58% in 50 min after 10 time cycles. For RhB, the photocatalytic degradation rate was remained up 87.63% in 90 min after ten time cycles. The detailed test results were showed in

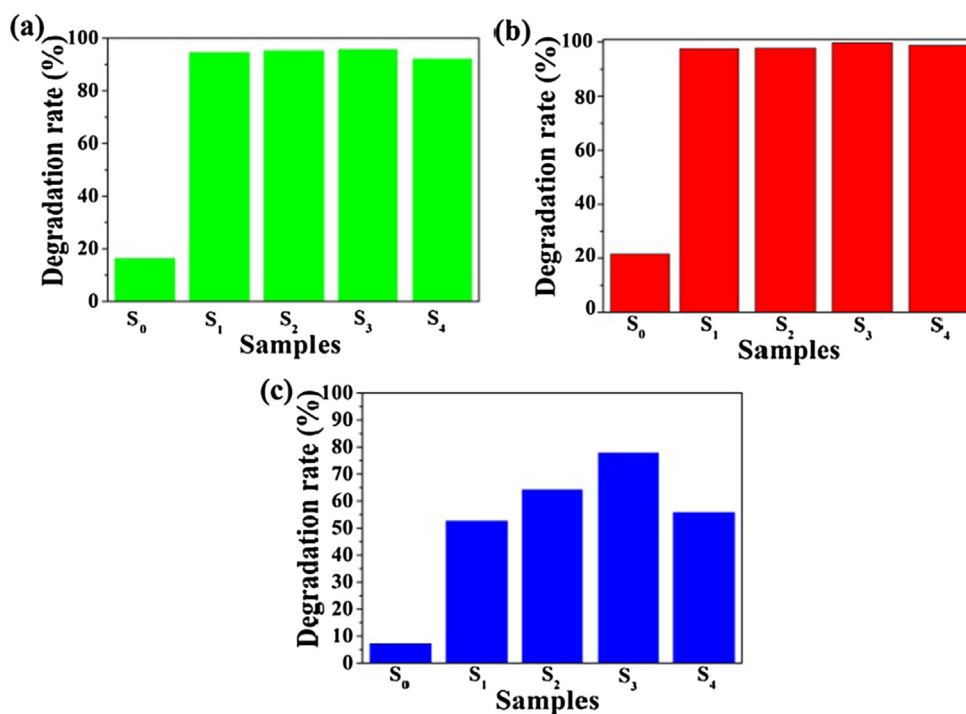


Fig. 5 Degradation rate histogram degradation of S₀, S₁, S₂, S₃ and S₄ samples to MO (a), MB (b), and RhB (c) under visible light irradiation for 50 min.

supporting information Table S1. It indicated that the prepared material had the better stability, and had the potential application value in environmental purification.

3.3. Photocatalytic mechanism

It is well known that the rapid photogenerated electrons-hole pair transfer rate and the slower photogenerated electron-hole recombination rates are benefit to improve the photocatalytic performance of the materials. The transfer efficiency of photogenerated electrons-hole pairs can be evaluated by PL spectrum. The materials have the lower PL luminescence intensity which will have the better photocatalyst performance. Fig. 9 presents the PL spectra of all catalysts which are excited by 371 nm light. A strong emission peak shows at around 437 nm which was attributed to the band-band PL phenomenon. It is found that the luminescent intensities are gradually decreased with the increase of g-C₃N₄ content, and the PL intensities are enhanced when the content of g-C₃N₄ is 40 wt%, which are inverse with the photocatalytic performances of samples. It is consistent with above theory. When the content of g-C₃N₄ is increased, the heterojunction interface may be reduced, the electron-hole recombination rate is increased, and the recombination center is increased.

Fig. 10(a) are the UV-Vis absorption spectra of all samples. The estimated band gaps of samples are showed in Fig. 10(b) which are obtained from UV-vis absorption spectra of the prepared samples. The band gap energy (E_g) values of all samples are calculated by the Kubelka-Munk theorem. The band gaps of S₀, S₁, S₂, S₃ and S₄ are 3.10, 2.51, 2.50, 2.47 and 2.48 eV, respectively. G-C₃N₄ exhibits light absorption over nearly

the visible light range, while SnO₂ merely responds to ultraviolet light. Doped g-C₃N₄, a visible light absorbance is observably enhanced for g-C₃N₄/SiO₂/SnO₂ composite.

Many reactive groups including ·OH, ·O₂⁻ and h⁺ are possible drawn into photocatalytic reaction, which are much significant to photocatalytic reaction. In order to verify their effect, isopropyl alcohol (IPA), 1,4-benzoquinone (BQ) and ethanedioic acid (K₂C₂O₄) are respectively used as scavenger of ·OH, ·O₂⁻ and h⁺, and the results are showed in Fig. 11(a). Photocatalytic effects of S₃ sample are significantly decreased when BQ is added to eliminate ·O₂⁻, which verifies that ·O₂⁻ is a much important active specie in the photocatalytic reaction. Degradation rate is reduced when IPA and K₂C₂O₄ are respectively added in photocatalytic system of S₃ sample, which suggests that h⁺ and ·OH play an equally significant role in the catalysis degradation. In order to prove the reactive species in photocatalytic degradation process, the electron spin resonance (ESR) is an ideal test method, which is used to detect reactive species under dark and visible light irradiation. No signal of ·O²⁻ is detected in dark, and the signals of ·O₂⁻ are detected when it is radiated by the visible light which is showed in Fig. 11(b). As showing in Fig. 11(c), the signal of ·OH has never appeared either in dark or in visible light conditions. The test results show that ·O₂⁻ can be generated, and ·OH almost is not produced during photocatalytic degradation.

When g-C₃N₄/SiO₂/SnO₂ nanocomposites are irradiated by visible light, the photoexcited electrons are generated in conduction band (CB) of g-C₃N₄, and finally transfer to the conduction band of SnO₂ in order to reduce potential energy. At same time, h⁺ are injected in the opposite direction for appropriate VB offsets, and the same amounts of h⁺ are enriched in the VB of g-C₃N₄, and h⁺ on VB of SnO₂ are

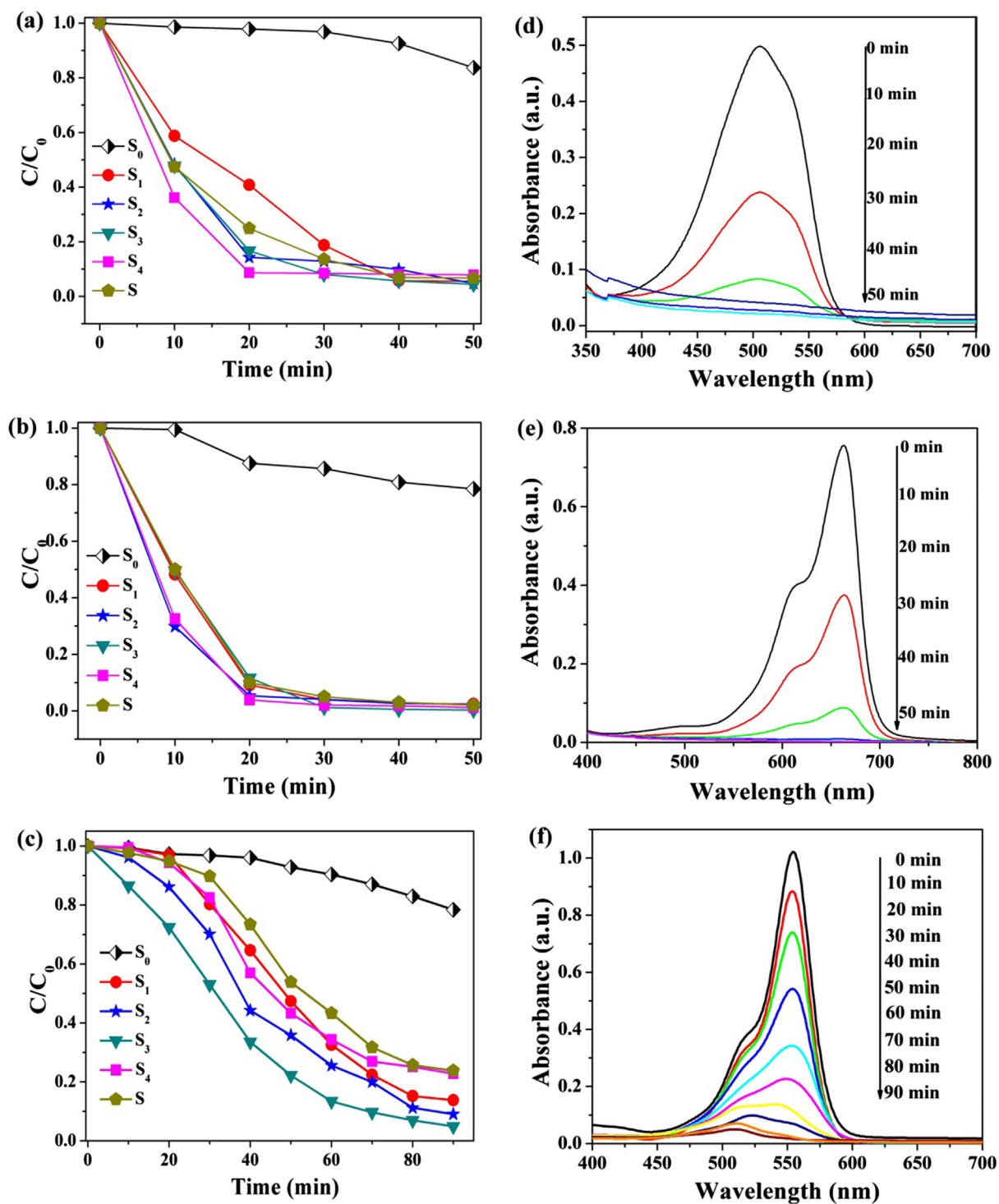


Fig. 6 Photocatalytic activity of samples to MO (a), MB (b) and RhB (c), and UV-Visible absorption spectrum of MO (d), MB (e) and RhB (f) under catalysis of S₃ in different visible light radiation time.

transferred to the VB of g-C₃N₄. Due to the presence of S₃ catalyst, the recombination rate of photo-generated electron-hole pairs in system is sharply reduced. Under the experimental condition, the electrons in CB of SnO₂ contact with adsorbed

O₂ to form $\cdot\text{O}_2^-$ on the surface. h^+ combines with water, and $\cdot\text{OH}$ is formed. By this way, electron-hole pair recombination is reduced. Because the $\cdot\text{OH}$ and $\cdot\text{O}_2^-$ are power oxidants, the organic pollutants can be decomposed effectively (Li et al., 2015).

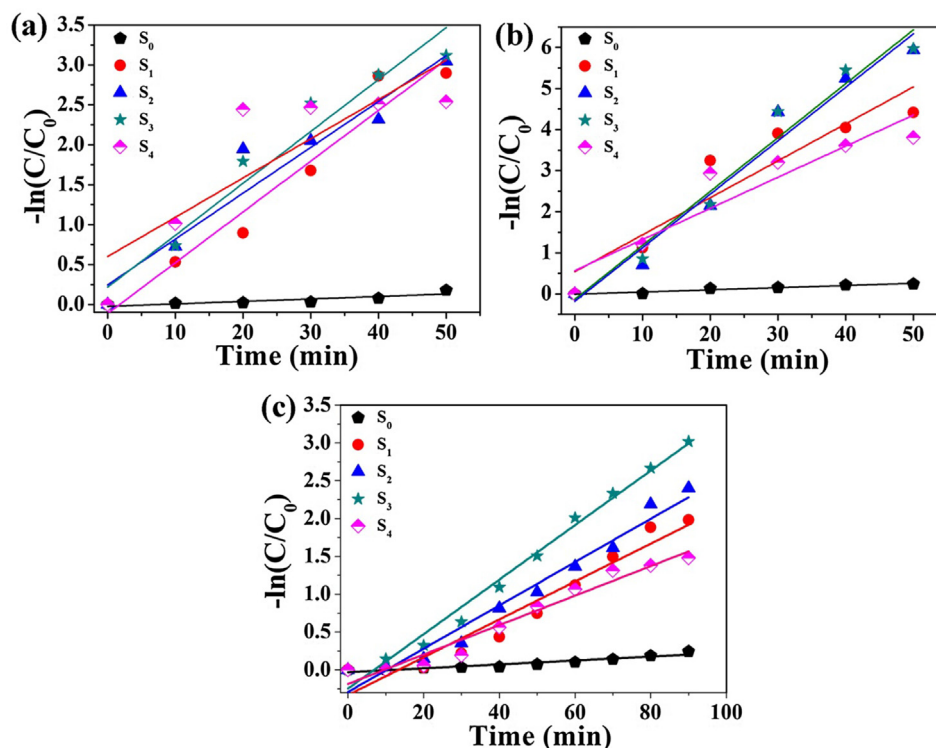


Fig. 7 Plots of $-\ln(C/C_0)$ versus irradiation time of S_0 , S_1 , S_2 , S_3 and S_4 samples to (a) MO, (b) MB and (c) RhB photocatalytic degradation.

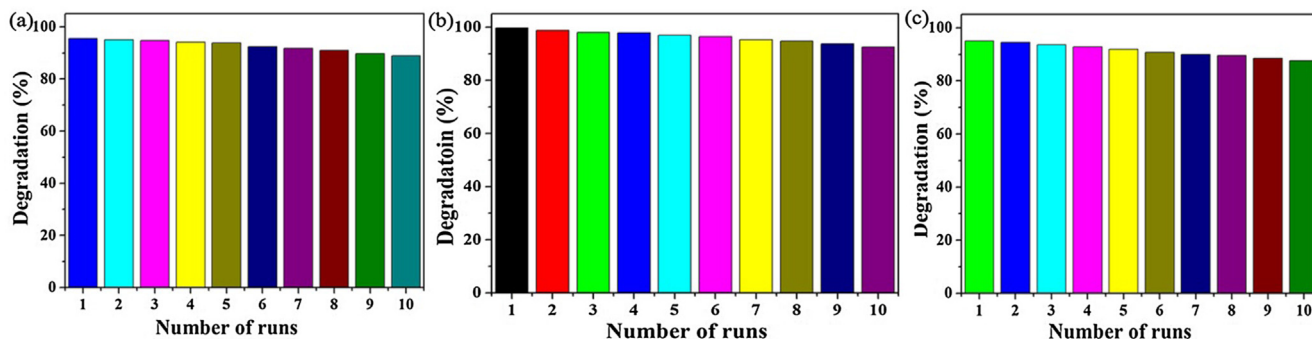


Fig. 8 Cycling stability test results of S_3 sample for MO (a), MB (b) and RhB (c).

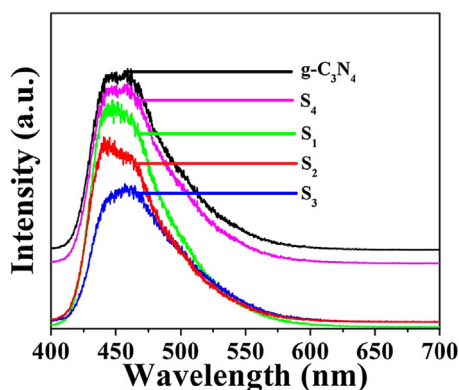


Fig. 9 Room temperature PL spectra of $g-C_3N_4$, S_1 , S_2 , S_3 and S_4 samples.

Schematic illustration of photocatalytic reaction and charge transfer of the S_3 sample under visible light irradiation is shown in Fig. 12.

In order to discuss SiO_2 effect, NaOH (2 mol/L) solution is used to remove SiO_2 from the sample, photocatalytic tests are carried out under the same conditions, the result is shown in Fig. 13. It is found that the photocatalytic effect is significantly reduced after the removal of SiO_2 , only 29.31% RhB has been degraded after 90 min. Zhou et al. (Zhou et al., 2013) indicated that SiO_2 can forbid the electron transfer effectively in $SiO_2-Ag-SiO_2-TiO_2$ composite. It is speculated that SiO_2 may forbid the electron effectively transfer during photocatalysis process in this study, which reduces the recombination rate of photogenerated electron-hole pairs in system. In this study, TEOS has catalysis for SnO_2 gelation, which make the structure of the prepared material become more loosen, defect

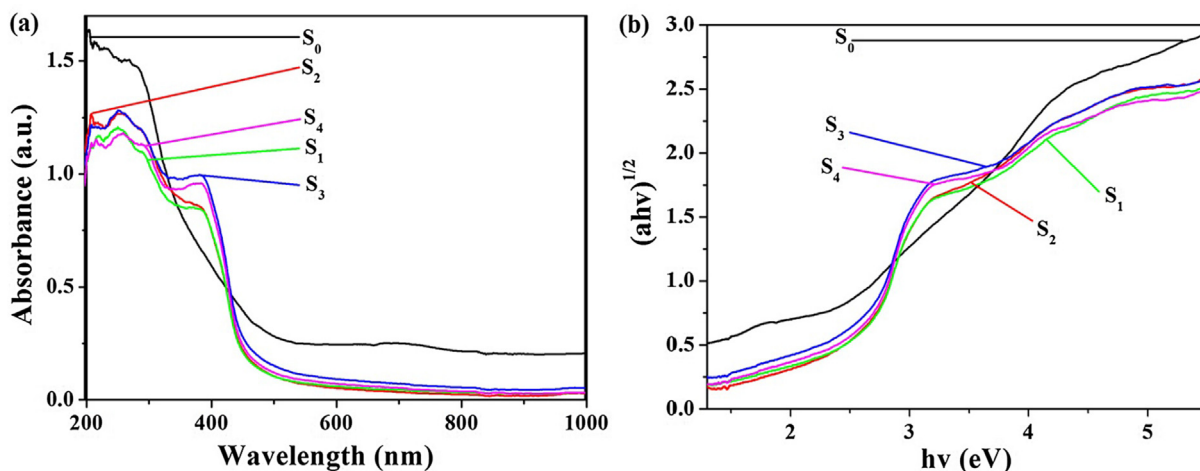


Fig. 10 (a) UV-Vis diffuse reflectance spectra and (b) $(\alpha hv)^{1/2}$ - $h\nu$ curves of S₀, S₁, S₂, S₃ and S₄ sample.

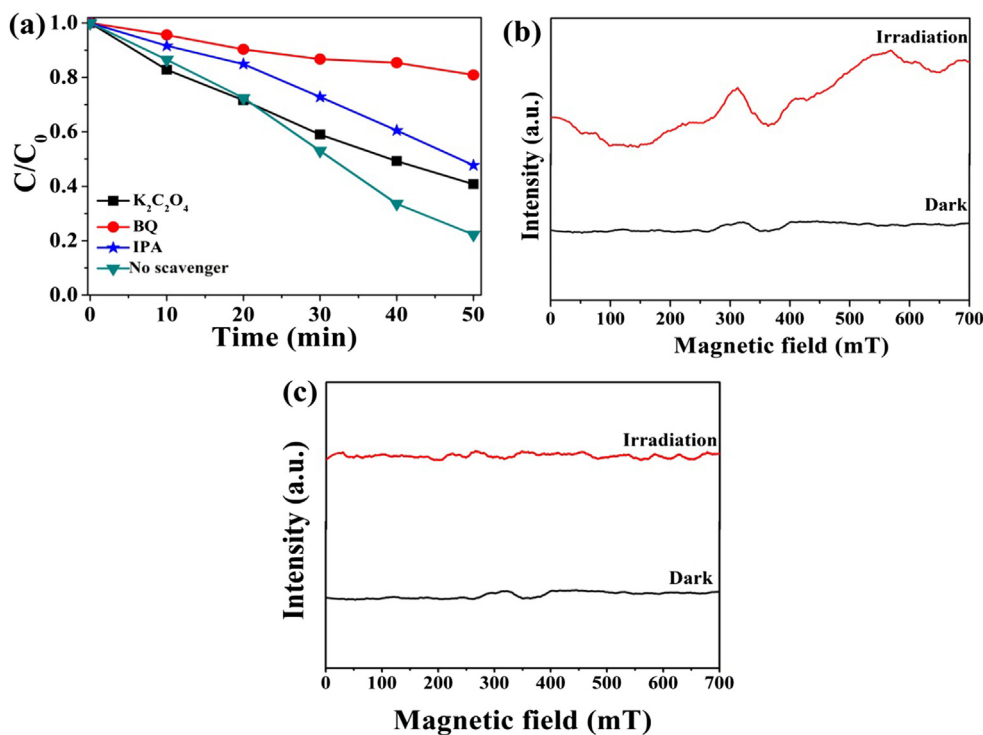


Fig. 11 (a) Photodegradation of RhB over S₃ sample with different quenchers; ESR spectra of radical actives trapped by DMPO for S₃ sample: (b) DMPO- $\cdot O_2^-$; (c) DMPO- $\cdot OH$.



Fig. 12 Schematic illustration of photocatalytic reaction and charge transfer of the S₃ sample under visible-light irradiation.

concentration increase, active site increase, and photocatalytic activity is enhanced. According to aerogel theory, the SiO₂ is porous structure in this system, which can not only increase sample's adsorb ability to organic contaminants, but also the porous SiO₂ provides a good high-speed channel for the migration of electrons, which effectively promotes the electron-hole separation ability in sample, thereby improves the photocatalytic performance of sample. Yu et al. has even studied the relevant research on this issue. (Yu et al., 2019) The loose porous structure of the prepared material was destroyed when the SiO₂ was removed, it lead to the structure collapse, and the photocatalytic performance of sample was dropped sharply.

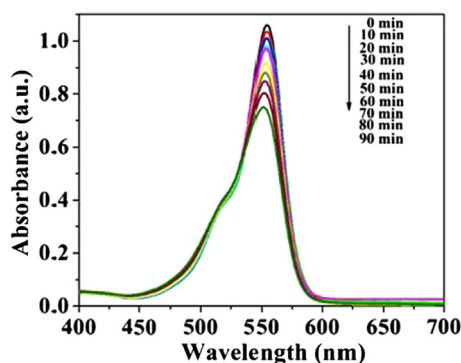


Fig. 13 UV-Visible absorption spectrum of Rh Bunder catalysis of S_3 removed SiO_2 sample with in different visible light radiation time.

4. Conclusions

In this study, $g-C_3N_4/SiO_2/SnO_2$ composite was synthesized by sol-gel hard-template method. The MO, MB and RhB photodegradation catalytic effects of $g-C_3N_4/SiO_2/SnO_2$ composite were inspected under visible light, which realized effective separation of photogenerated electron-hole pairs. When loaded $g-C_3N_4$ was 30 wt%, the highest photocatalytic activity was obtained. This work provided a facile method for synthesis organic-inorganic catalytic material, and $g-C_3N_4/SiO_2/SnO_2$ heterojunction structure materials could serve as a promising candidate as the catalytic material in pollution treatment applications.

Acknowledgements

We gratefully acknowledge the support of the work by the National Natural Science Foundation of China (Grant No. 51572034).

Declaration of Competing Interest

All authors declare that they have no conflict of interest.

Appendix A. Supplementary material

Supporting information contains the degradation profile of RhB over S_3 sample in visible light exposed to 50 min in Fig. S1, and the photocatalytic degradation rate of S_3 sample for MO, MB and RhB in cycling experiments in Table S1. Supplementary data to this article can be found online at <https://doi.org/10.1016/j.arabj.2019.07.009>.

References

- Chen, W.H., Song, K.M., Mi, L.W., Feng, X.M., Zhang, J.M., Cui, S. Z., Liu, C.T., 2017. Synergistic effect induced ultrafine SnO_2 /graphene nanocomposite as an advanced lithium/sodium-ion batteries anode. *J. Mater. Chem. A* 5, 10027–10038.
- Davis, M., Hikal, W.M., 2012. Aerogel nanocomposites of $ZnO-SnO_2$ as efficient photocatalysts for the degradation of rhodamine B. *Catal. Sci. Technol.* 2, 922–924.
- Du, H.Y., Wang, J., Sun, Y.H., Yao, P.J., Li, X.G., Yu, N.S., 2015. Sens. Investigation of gas sensing properties of SnO_2/In_2O_3 heteronanofibers treated by oxygen plasma. *Actuat. B: Chem.* 206, 753–763.
- Hao, R.R., Wang, G.H., Jiang, C.J., Tang, H., Xu, Q.C., 2017. In situ hydrothermal synthesis of $g-C_3N_4/TiO_2$ heterojunction photocatalysts with high specific surface area for Rhodamine B degradation. *Appl. Surf. Sci.* 411, 400–410.
- He, K.L., Xie, J., Luo, X.Y., Wen, J.Q., Ma, S., Li, X., Fang, Y.P., Zhang, X.C., 2017. Enhanced visible light photocatalytic H_2 production over Z-scheme $g-C_3N_4$ nanosheets/ WO_3 nanorods nanocomposites loaded with $Ni(OH)_x$ cocatalysts. *Chinese J. Catal.* 38, 240–252.
- Huang, X., Shang, L., Chen, S., Xia, J., Qi, X.P., Wang, X.C., Zhang, T.R., Meng, X.M., 2013. Type-II ZnO nanorod- SnO_2 nanoparticle heterostructures: characterization of structural, optical and photocatalytic properties. *Nanoscale* 5, 3828–3833.
- Jallouli, N., Elghniji, K., Trabelsi, H., Ksibi, M., 2019. Photocatalytic degradation of paracetamol on TiO_2 nanoparticles and TiO_2 /cellulosic fiber under UV and sunlight irradiation. *Arab. J. Chem.* 10, S3640–S3645.
- Jiang, H.Y., Liu, G.G., Wang, T., Li, P., Liu, J., Ye, J.H., 2015. In situ construction of $\alpha-Bi_2O_3/g-C_3N_4/\beta-Bi_2O_3$ composites and their highly efficient photocatalytic performances. *RSC Adv.* 5, 92963–92969.
- Kar, A., Kundu, S., Patra, A., 2012. Photocatalytic properties of semiconductor SnO_2/CdS heterostructure. *RSC Adv.* 2, 10222–10230.
- Kong, L.G., Dong, Y.M., Jiang, P.P., Wang, G.L., Zhang, H.Z., Zhao, N., 2016. Light-assisted rapid preparation of $Ni/g-C_3N_4$ magnetic composite for robust photocatalytic H_2 evolution from water. *J. Mater. Chem. A* 4, 9998–10007.
- Kuang, P.Y., Su, Y.Z., Chen, G.F., Luo, Z., Xing, S.Y., Li, N., Liu, Z. Q., 2015. $g-C_3N_4$ decorated ZnO nanorod arrays for enhanced photoelectrocatalytic performance. *Appl. Surf. Sci.* 358, 296–303.
- Kumar, S., Baruah, A., Tonda, S., Kumar, B., Shanker, V., Sreedhar, B., 2014. Cost-effective and eco-friendly synthesis of novel and stable N-doped $ZnO/g-C_3N_4$ core-shell nanoplates with excellent visible-light responsive photocatalysis. *Nanoscale* 6, 4830–4842.
- Li, Y.F., Fang, L., Jin, R.X., Yang, Y., Fang, X., Song, S.Y., 2015. Preparation and enhanced visible light photocatalytic activity of novel $g-C_3N_4$ nanosheets loaded with Ag_2CO_3 nanoparticles. *Nanoscale* 7, 758–764.
- Li, Z.D., Zhou, Y., Song, J.C., 2013. ersatile nanobead- scaffolded N- SnO_2 mesoporous microspheres: one - step synthesis and superb performance in dye - sensitized solar cell, gas sensor, and photocatalytic degradation of dye. *J. Mater. Chem.* 1, 524–531.
- Lin, Y., Li, C., Wei, W., Li, Y.J., Wen, S.P., Sun, D.M., Chen, Y., Ruan, S.P., 2015. A new type of acetylene gas sensor based on a hollow heterostructure. *RSC Adv.* 5, 61521–61527.
- Liu, H.R., Hu, C.J., Zhai, H.F., Yang, J.E., Liu, X.G., Jia, H.S., 2017. Fabrication of $In_2O_3/ZnO@Ag$ nanowire ternary composites with enhanced visible light photocatalytic activity. *RSC Adv.* 7, 37220–37229.
- Liu, Y., Jiao, Y., Zhang, Z.L., Qu, F.Y., Umar, A., Wu, X., 2014. Hierarchical SnO_2 nanostructures made of intermingled ultrathin nanosheets for environmental remediation. *ACS Appl. Mater. Interfaces* 6, 2174–2184.
- Liu, S.Q., Xie, M.J., Li, Y.X., Guo, X.F., Ji, W.J., Ding, W.P., Au, C. T., 2010. Novel sea urchin-like hollow core-shell SnO_2 superstructures: Facile synthesis and excellent ethanol sensing performance. *Sens. Actuat. B: Chem.* 151, 229–235.
- Mohamed, R.M., McKinney, D.L., Sigmund, W.M., 2012. Enhanced nanocatalysts. *Mater. Sci. Eng. R* 73, 1–13.
- Nadarajan, R., Abu Bakar, W.A.W., Ali, R., Ismail, R., 2018. Photocatalytic degradation of 1,2-dichlorobenzene using immobi-

- lized TiO₂/SnO₂/WO₃ photocatalyst under visible light: Application of response surface methodology. *Arab. J. Chem.* 11, 34–47.
- Naseri, A., Samadi, M., Pourjavadi, A., Moshfegh, A.Z., Ramakrishna, S., 2017. Graphitic carbon nitride (g-C₃N₄) - based photocatalysts for solar hydrogen generation: recent advances and future development directions. *J. Mater. Chem. A* 5, 23406–23433.
- Park, J.T., Lee, C.S., Kim, J.H., 2014. One-pot synthesis of hierarchical mesoporous SnO₂ spheres using a graft copolymer: enhanced photovoltaic and photocatalytic performance. *RSC Adv.* 4, 31452–31461.
- Qi, Q., Wang, P.P., Zhao, J., Feng, L.L., Zhou, L.J., Xuan, R.F., Liu, Y.P., Li, G.D., 2014. SnO₂ nanoparticle-coated In₂O₃ nanofibers with improved NH₃ sensing properties. *Sens. Actuat. B: Chem.* 194, 440–446.
- Rakibuddin, M., Ananthakrishnan, R., 2017. Fabrication of graphene aerosol hybridized coordination polymer derived CdO/SnO₂ heteronanostructure with improved visible light photocatalytic performance. *Sol. Energ. Mat. Sol. C.* 162, 62–71.
- Rashid, J., Barakat, M.A., Salah, N., Habib, S.S., 2014. Ag/ZnO nanoparticles thin films as visible light photocatalysts. *RSC Adv.* 4, 56892–56899.
- Reddy, M.J., Shanmugaraj, A.M., Ryu, S.H., 2016. Synergistic effect induced ultrafine SnO₂/graphene nanocomposite as an advanced lithium/sodium-ion batteries anode. *Nanoscale* 8, 471–482.
- Shi, R., Cao, Y.H., Bao, Y.J., Zhao, Y.F., Waterhouse, G.I.N., Fang, Z.Y., Wu, L.Z., Tung, C.H., Yin, Y.D., Zhang, T.R., 2017. Self-assembled Au/CdSe nanocrystal clusters for plasmon mediated photocatalytic hydrogen evolution. *Adv. Mater.* 29, 1700803.
- Son, D.Y., Lee, C.R., Shin, H.W., Jang, I.H., Jung, H.S., Ahn, T.K., Park, N.G., 2015. Understanding the role of the dye/oxide interface via SnO₂-based MK-2 dye - sensitized solar cells. *Phys. Chem. Chem. Phys.* 17, 15193–15200.
- Sun, L.M., Qi, Y., Jia, C.J., Jin, Z., Fan, W.L., 2014. Enhanced visible-light photocatalytic activity of g-C₃N₄/Zn₂GeO₄ heterojunctions with effective interfaces based on band match. *Nanoscale* 6, 2649–2659.
- Thomas, A., Fischer, A., Goettmann, F., Antonietti, M., Muller, J.O., Schlogl, R., Carisson, J.M., 2008. ChemInform abstract: graphitic carbon nitride materials: variation of structure and morphology and their use metal-free catalysts. *J. Mater. Chem.* 18, 4893–4908.
- Tian, Q.Y., Wu, W., Sun, L.L., Yang, S.L., Lei, M., Zhou, J., Liu, Y., Xiao, X.H., Ren, F., Jiang, C.Z., 2014. Tube-like ternary α -Fe₂O₃@SnO₂@Cu₂O sandwich heterostructures: synthesis and enhanced photocatalytic properties. *ACS Appl. Mater. Interfaces* 6, 13088–13097.
- Wang, S., Li, C., Wang, T., Zhang, P., Li, A., Gong, J., 2014. Controllable synthesis of nanotube-type graphitic C₃N₄ and their visible-light photocatalytic and fluorescent properties. *J. Mater. Chem. A* 2, 2885–2890.
- Wang, P., Lu, N., Su, Y., Liu, N., Yu, H.T., Li, J., Wu, Y., 2017. Fabrication of WO₃@g-C₃N₄ with core@shell nanostructure for enhanced photocatalytic degradation activity under visible light. *Appl. Surf. Sci.* 423, 197–204.
- Wang, Z.L., Wu, W.Z., 2013. Nanotechnology-enabled energy harvesting for self-powered micro – nanosystems. *Angew. Chem. Int. Ed.* 51, 1170–11721.
- Wei, X.N., Wang, H.L., Wang, X.K., 2017. Facile fabrication of mesoporous g-C₃N₄/TiO₂ photocatalyst for efficient degradation of DNBP under visible light irradiation. *Appl. Surf. Sci.* 426, 1271–1280.
- Wen, J.Q., Xie, J., Chen, X.B., Li, X., 2017. A review on g-C₃N₄-based photocatalysts. *Appl. Surf. Sci.* 391, 72–123.
- Wu, F.J., Li, X., Liu, W., Zhang, S.T., 2017. Highly enhanced photocatalytic degradation of methylene blue over the indirect all-solid-state Z-scheme g-C₃N₄-RGO-TiO₂ nanoheterojunctions. *Appl. Surf. Sci.* 405, 60–70.
- Wu, W., Zhang, S.F., Ren, F., Xiao, X.H., Zhou, J., Jiang, C.Z., 2011. Controlled synthesis of magnetic iron oxides@SnO₂ quasi-hollow core-shell heterostructures: formation mechanism, and enhanced photocatalytic activity. *Nanoscale* 3, 4676–4684.
- Xia, L., Zhang, X.Y., Yang, Y.N., Zhang, J., Zhong, B., Zhang, T., Wang, H.T., 2018. Enhanced electromagnetic wave absorption properties of laminated SiC_{NW}-C_f/thium-aluminum-silicate (LAS) composites. *J. Alloy. Compd.* 748, 154–162.
- Xu, Q.L., Zhu, B.C., Jiang, C.J., Cheng, B., Yu, J.G., 2018. Constructing 2D/2D Fe₂O₃/g-C₃N₄ direct Z-scheme photocatalysts with enhanced H₂ generation performance. *Sol. RRL* 2, 1800006.
- Yan, Y.X., Yang, H., Zhao, X.X., Li, R.S., Wang, X.X., 2018. Enhanced photocatalytic activity of surface disorder-engineered CaTiO₃. *Mater. Res. Bull.* 105, 286–290.
- Yang, Y.N., Xia, L., Zhang, T., Shi, B., Huang, L.N., Zhong, B., Zhang, X.Y., Wang, H.T., Zhang, J., Wen, G.W., 2018. Fe₃O₄@-LAS/RGO composites with a multiple transmission-absorption mechanism and enhanced electromagnetic wave absorption performance. *Chem. Eng. Jour.* 352, 510–518.
- You, H.J., Liu, R., Liang, C.C., Yang, S.C., Wang, F., Lu, X.G., Ding, B.J., 2013. Gold nanoparticle doped hollow SnO₂ supersymmetric nanostructures for improved photocatalysis. *J. Mater. Chem. A* 1, 4097–4104.
- Yu, C.L., He, H.B., Liu, X.Q., Zeng, J.L., Liu, Z., 2019. Novel SiO₂ nanoparticle-decorated BiOCl nanosheets exhibiting high photocatalytic performances for the removal of organic pollutants. *Chinese J. Catal.* 40, 1212–1221.
- Yu, H.J., Shi, R., Zhao, Y.X., Biao, T., Zhao, Y.F., Zhou, C., Waterhouse, G.I.N., Wu, L.Z., Tung, C.H., Zhang, T.R., 2017. Alkali-assisted synthesis of nitrogen deficient graphitic carbon nitride with tunable band structures for efficient visible-light-driven hydrogen evolution. *Adv. Mater.* 29, 1605148.
- Zhang, S.F., Ren, F., Wu, W., Zhou, J., Xiao, X.H., Sun, L.L., Liu, Y., Jiang, C.Z., 2013. Controllable synthesis of recyclable core-shell γ -Fe₂O₃@SnO₂ hollow nanoparticles with enhanced photocatalytic and gas sensing properties. *Phys. Chem. Chem. Phys.* 15, 8228–8236.
- Zhao, H., Ding, X.L., Zhang, B., Li, Y.X., Wang, C.Y., 2017. Enhanced photocatalytic hydrogen evolution along with byproducts suppressing over Z-scheme Cd_xZn_{1-x}S/Au/g-C₃N₄ photocatalysts under visible light. *Sci. Bull.* 62, 602–609.
- Zhao, X.X., Yang, H., Li, S.H., Cui, Z.M., Zhang, C.R., 2018. Synthesis and theoretical study of large-sized Bi₄Ti₃O₁₂ square nanosheets with high photocatalytic activity. *Mater. Res. Bull.* 107, 180–188.
- Zheng, C.X., Yang, H., 2018. Assembly of Ag₃PO₄ nanoparticles on rose flower-like Bi₂WO₆ hierarchical architectures for achieving high photocatalytic performance. *J. Mater. Sci.: Mater. Electron.* 29, 29291–29300.
- Zheng, L.H., Yu, X.J., Long, M.C., Li, Q.L., 2017. Humic acid-mediated visible-light degradation of phenol on phosphate-modified and nafion-modified TiO₂ surface. *Chinese J. Catal.* 38, 2076–2084.
- Zhou, J., Ren, F., Zhang, S.F., Wu, W., Xiao, X.H., Liu, Y., Jiang, C. Z., 2013. SiO₂-Ag-SiO₂-TiO₂ multi-shell structures: plasmon enhanced photocatalysts with wide-spectral-response. *J. Mater. Chem. A* 1, 13128–13138.
- Zhou, C., Shi, R., Shang, L., Wu, L.Z., Tung, C.H., Zhang, T.R., 2018. Template-free large-scale synthesis of g-C₃N₄ microtubes for enhanced visible light-driven photocatalytic H₂ production. *Nano Res.* 11, 3462–3468.